The non-evolving internal structure of early-type galaxies: the case study SDSS J0728+3835 at $z = 0.206$

Matteo Barnabè,[1,2]★ Matthew W. Auger,[2] Tommaso Treu,[2]† Léon V. E. Koopmans,[3] Adam S. Bolton,[4,5]‡ Oliver Czoske[3] and Raphaël Gavazzi[6]

[1]*Kavli Institute for Particle Astrophysics and Cosmology, Stanford University, 452 Lomita Mall, Stanford, CA 94035-4085, USA*
[2]*Department of Physics, University of California, Santa Barbara, CA 93101, USA*
[3]*Kapteyn Astronomical Institute, University of Groningen, PO Box 800, 9700 AV Groningen, the Netherlands*
[4]*Department of Physics and Astronomy, University of Utah, 115 South 1400 East, Salt Lake City, UT 84112, USA*
[5]*Institute for Astronomy, University of Hawai'i, 2680 Woodlawn Dr., Honolulu, HI 96822, USA*
[6]*Institut d'Astrophysique de Paris, CNRS, UMR 7095, Université Pierre et Marie Curie, 98bis Bd Arago, 75014 Paris, France*

ABSTRACT

We study the internal dynamical structure of the early-type lens galaxy SDSS J0728+3835 at $z = 0.206$. The analysis is based on two-dimensional kinematic maps extending out to 1.7 effective radii obtained from Keck spectroscopy, on lensing geometry and on stellar mass estimates obtained from multiband *Hubble Space Telescope* imaging. The data are modelled under the assumptions of axial symmetry supported by a two-integral distribution function, by applying the combined gravitational lensing and stellar dynamics code CAULDRON and by yielding high-quality constraints for an early-type galaxy at cosmological redshifts. Modelling the total density profile as a power law of the form $\rho_{\rm tot} \propto 1/r^{\gamma'}$, we find that it is nearly isothermal (logarithmic slope $\gamma' = 2.08^{+0.04}_{-0.02}$) and quite flattened (axial ratio $q = 0.60^{+0.08}_{-0.03}$). The galaxy is mildly anisotropic ($\delta = 0.08 \pm 0.02$) and shows a fair amount of rotational support, in particular towards the outer regions. We determine a dark matter fraction lower limit of 28 per cent within the effective radius. The stellar contribution to the total mass distribution is close to maximal for a Chabrier initial mass function (IMF), whereas for a Salpeter IMF the stellar mass exceeds the total mass within the galaxy inner regions. We find that the combination of a Navarro, Frenk and White dark matter halo with the maximally rescaled luminous profile provides a remarkably good fit to the total mass distribution over a broad radial range. Our results confirm and expand the findings of the Sloan Lens ACS Survey for early-type galaxies of comparable velocity dispersion ($\sigma_{\rm SDSS} = 214 \pm 11$ km s^{-1}). The internal structure of SDSS J0728 is consistent with that of local early-type galaxies of comparable velocity dispersion as measured by the Spectrographic Areal Unit for Research on Optical Nebulae (SAURON) project, suggesting lack of evolution in the past two billion years.

Key words: gravitational lensing: strong – galaxies: elliptical and lenticular, cD – galaxies: kinematics and dynamics – galaxies: structure.

1 INTRODUCTION

Unveiling the mass distribution, dynamical structure and dark matter content of early-type galaxies is of great interest both as a subject in its own right, considering their importance in the local Universe, where a large fraction of the total stellar mass is contained within E/S0 systems (Fukugita, Hogan & Peebles 1998), and in order to provide stringent tests for the galaxy formation and evolution models.

It is not surprising therefore that nearby early-type galaxies have been the object of intense study during the last decades, by taking advantage of the diverse available observational tracers. These include stellar kinematics (see e.g. Saglia, Bertin & Stiavelli 1992; Franx, van Gorkom & de Zeeuw 1994; Rix et al. 1997; Loewenstein & White 1999; Gerhard et al. 2001; Borriello, Salucci & Danese 2003; Cappellari et al. 2007; Thomas et al. 2007b; Weijmans et al. 2009), globular clusters and planetary nebulae kinematics (e.g. Côté

★ E-mail: mbarnabe@stanford.edu
† Packard Research Fellow.
‡ Beatrice Watson Parent Fellow.

et al. 2003; Romanowsky et al. 2003; de Lorenzi et al. 2008), the occasional H I disc or ring (e.g. Franx et al. 1994; Weijmans et al. 2008) and hot X-ray emission (e.g. Matsushita et al. 1998; Fukazawa et al. 2006; Humphrey et al. 2006; Humphrey & Buote 2010). The general picture emerging from many of these studies is that the total mass density profile of ellipticals can be well described by a power-law form close to $\rho_{tot} \propto 1/r^2$, often referred to as the isothermal profile. Moreover, while the inner regions of early-type galaxies are clearly dominated by the stellar component, the dark matter component is usually found to play already a non-negligible role, with fractions of approximately 10–40 per cent of the total mass within an effective radius. Studies based on stellar population and dynamical models (e.g. Padmanabhan et al. 2004) indicate that the dark matter fraction increases with the mass of the galaxy, a trend that is more conspicuous in the case of slow-rotator ellipticals (Tortora et al. 2009).

The analysis of early-type galaxies beyond the local Universe, i.e. beyond redshift $z \approx 0.1$, holds great promise in view of understanding the structural evolution of these objects, but it also presents several difficulties which hinder the application of traditional techniques. Stellar dynamics studies, in particular, are limited by the degeneracy between the galaxy mass profile and the anisotropy of the stellar velocity dispersion tensor. Taking into account higher order velocity moments can provide a solution (see Gerhard 1993; van der Marel & Franx 1993; Łokas & Mamon 2003), but unfortunately carrying out such measurement for distant systems is not viable with the current instruments on 8–10-m class telescopes.

However, galaxies at $z \gtrsim 0.1$ have a far greater chance of acting as strong gravitational lenses (Turner, Ostriker & Gott 1984), thus providing a very helpful additional diagnostic tool. This is particularly valuable since it allows an accurate and robust determination of the total mass enclosed, in projection, within the region delimited by the Einstein radius (Kochanek 1991). Unfortunately, the diagnostic power of strong lensing to constrain the internal mass distribution of the deflector is limited, chiefly by the mass-sheet and mass-slope degeneracies (Falco, Gorenstein & Shapiro 1985; Wucknitz 2002), although the latter can be partially overcome by studying spatially extended lensed sources (e.g. Warren & Dye 2003; Suyu et al. 2010). A very effective way to overcome these difficulties and robustly recover various structural properties of the galaxy is to combine the gravitational lensing analysis with the complementary constraints provided by stellar dynamics (see Koopmans & Treu 2002, 2003; Treu & Koopmans 2002a,b, 2004; Barnabè & Koopmans 2007, hereafter BK07; e.g. Rusin & Kochanek 2005; Jiang & Kochanek 2007; van de Ven et al. 2008; Trott et al. 2010; Grillo et al. 2010 for further applications of this approach).

Up to very recently, the availability of only a handful of lens galaxies suitable for the joint analysis represented a major limitation. This concern has been dispelled by the Sloan Lens ACS Survey (SLACS; Bolton et al. 2006; 2008a,b; Koopmans et al. 2006, 2009; Treu et al. 2006, 2009; Gavazzi et al. 2007, 2008; Auger et al. 2009), which has led to the discovery of a large and homogeneous sample of almost a hundred strong gravitational lenses, mostly early-type galaxies, in the redshift range of $z \approx 0.05$–0.5. For a subset of about 30 SLACS systems, the data set is complemented by two-dimensional kinematic maps of the lens obtained from spectroscopic observations carried out either with the Very Large Telescope (VLT) instrument Visible Multi-Object Spectrograph (VIMOS) or with the Low Resolution Imager and Spectrograph (LRIS; see Oke et al. 1995) mounted on the Keck-I telescope. This has provided further motivation to expand the combined analysis technique into

a more general and self-consistent method which makes full use of the available data sets (i.e. surface brightness distribution of both the lensed source and the lens galaxy, and two-dimensional kinematic maps of the latter) and is coherently embedded in the framework of Bayesian statistics (BK07). The current implementation of the method, the CAULDRON code – based on the assumptions of axial symmetry and two-integral stellar distribution function (DF) for the lens galaxy – has been used to conduct an in-depth study of a SLACS subsample of six systems representative of the survey in terms of redshifts and velocity dispersions (see Czoske et al. 2008; Barnabè et al. 2009b, hereafter B09). As shown in those works, the more sophisticated approach makes it possible to extract much more information out of the data set, allowing us to recover, in addition to the slope of the total density profile, several other important properties of the lens galaxies, including the flattening of the density distribution, lower limits for the dark matter fraction at different radii and insights into the dynamical structure (angular momentum, anisotropy, contribution of rotation and random motions). These quantities are all of relevance to the formation history of these galaxies.

In this paper, we carry out a detailed combined lensing and dynamics analysis of the SLACS system SDSS J0728+3835, employing the CAULDRON algorithm. The lens is an early-type galaxy at $z = 0.206$, with an aperture-averaged velocity dispersion $\sigma = 214 \pm 11$ km s^{-1} measured from Sloan Digital Sky Survey (SDSS) spectroscopy and a half-light radius $R_e = 1.78$ arcsec in the I band. The background source is located at $z = 0.688$ and the Einstein radius is $R_{Einst} = 1.25$ arcsec. With respect to the systems considered in Czoske et al. (2008) and B09, all followed up with the VLT VIMOS integral-field unit (IFU), the main difference in the observables lies in the kinematic data set: the SDSS J0728 velocity moment maps are obtained from LRIS Keck long-slit spectroscopic observations, using three slits parallel to the major axis and offset along the minor axis, in order to mimic integral-field capabilities. Remarkably, this kinematic data set extends significantly farther than those of the previously examined systems, reaching up to $1.7R_e$, thus providing us important constraints beyond the inner regions of the galaxy. Moreover, for the first time, we use the stellar masses determined from stellar population analysis (Auger et al. 2009) to set the normalization of the luminous mass distribution of the lens galaxy, enabling us to disentangle the luminous and dark matter contributions and to compare different choices of the initial mass function (IMF).

The paper is organized as follows: after introducing the data set in Section 2, we present and discuss the results of the combined analysis in Section 3 and draw conclusions in Section 4.

Throughout this paper, we adopt a concordance Λ cold dark matter model described by $\Omega_M = 0.3$, $\Omega_\Lambda = 0.7$ and $H_0 = 100\,h$ km s^{-1} Mpc^{-1} with $h = 0.7$, unless stated otherwise.

2 OBSERVATIONS

2.1 High-resolution imaging data

The lensing analysis requires deep high-resolution imaging data, and this is provided by SLACS' *Hubble Space Telescope* (*HST*) imaging. In particular, SLACS has obtained one *HST* orbit (≈ 2200 s) of data in the F814W filter. The data are processed as described in Bolton et al. (2008a); to briefly summarize, the four individual exposures are background subtracted, cosmic-ray-cleaned, registered, resampled to an output grid with square pixels that are 0.05 arcsec on a side, and stacked with an additional cosmic-ray-rejection step. Synthetic point-spread function (PSF)

images created with TinyTim are likewise resampled and combined to create a composite model PSF for the output image.

The light distribution of the galaxy is then fitted with a B-spline model (e.g. Bolton et al. 2008a) and this model, convolved with the seeing present during the spectroscopic observations, is used as the input surface brightness distribution for the dynamics modelling. The residual image (the B-spline model subtracted from the data image) contains the flux from the lensed background source and is used as a lensing constraint on the mass model of the lens galaxy (see BK07 for details). The galaxy-subtracted image is shown in the bottom-right panel of Fig. 4.

2.2 Pseudo-IFU spectroscopy

Our previous joint lensing and dynamics studies used VLT-VIMOS IFU spectroscopy to generate resolved stellar kinematic maps. In this study we employ 'pseudo-IFU' spectroscopy, which consists of dithering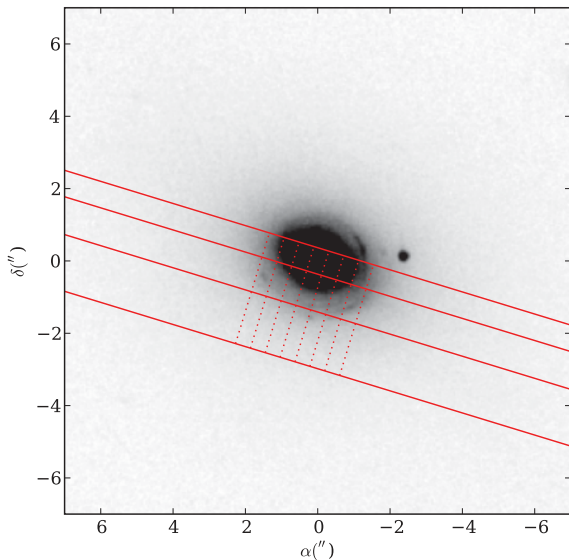 a traditional longslit in the spectral direction over the target galaxy to provide spatially resolved kinematic data perpendicular to the slit direction in addition to the spatial information that is obtained along each slit (see Fig. 1). This technique yields significantly fewer spaxels per exposure than proper IFU spectroscopy, but the throughput from the longslit is a factor of a few larger than the IFU throughput and we are therefore able to efficiently produce kinematic maps, despite the less efficient way of sampling the kinematic field. Additionally, we are more sensitive to the low-surface brightness outer regions of the galaxy and can therefore extend our kinematic maps to larger radii than is possible with the IFU data.

The spectroscopic data for SDSS J0728 were obtained with LRIS on Keck I during the nights of 2006 December 22 and 23. The observing conditions were clear with $\approx$0.8-arcsec seeing, and we used the 460 dichroic to split the beam into the blue and red sides of the spectrograph. Here we only use data from the red side, which employed the 900/5500 grating with a dispersion scale of 0.85 Å pixel^{-1}. Three slit positions aligned along the semimajor axis of the galaxy were observed, including two 900-s exposures with a 0.7-arcsec slit positioned on the centre of the galaxy, four 1200-s exposures with a 1-arcsec slit offset 0.85 arcsec from the centre of the galaxy and four 1800-s exposures with a 1.5-arcsec slit offset 2.1 arcsec from the centre of the galaxy. The data were reduced using custom Python scripts (for details, see Suyu et al. 2010) and one-dimensional spectra were extracted from apertures of a width of 2 pixels ($\approx$0.43 arcsec) at seven points along each slit as indicated in Fig. 1, yielding 21 spectra in total (e.g. Fig. 2).

The stellar velocity dispersion and velocity offset were computed for each spectrum as in Suyu et al. (2010) using the rest-frame wavelength range from 4200 to 5450 Å and errors were determined from Markov chain Monte Carlo simulations. The resulting velocity and velocity dispersion profiles for each slit position are shown in Fig. 3. We compare our data with the velocity dispersion derived from the SDSS spectrum by combining the 14 spectra from the inner two slits and determining a composite velocity dispersion. This is found to be 236 km s^{-1}, rather larger than the value of 214 km s^{-1} found for the SDSS spectrum. We have re-analysed the SDSS spectrum and find $\sigma = 212$ km s^{-1}, but if we mask the O II lines (as is done in the analysis of the Keck spectra) we find $\sigma = 225$ km s^{-1}. This is still somewhat lower than, although consistent within the errors with, the central velocity dispersion derived from the composite Keck spectrum. However, we might expect the SDSS value to be lower due to poor seeing pushing more flux from large radii (where the velocity dispersion is lower) into the SDSS fibre aperture.
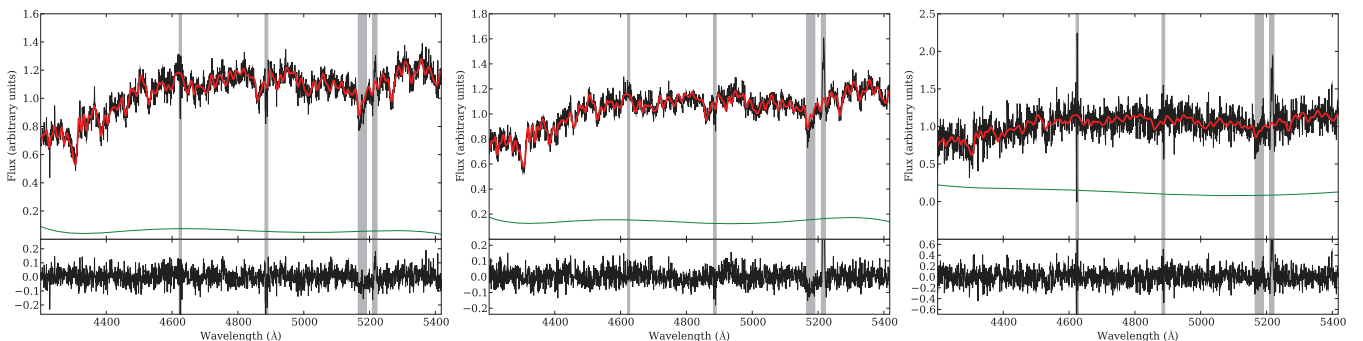

Figure 1. *HST* F814W image of SDSS J0728 with the slit locations overplotted as solid lines. The most narrow slit (0.7 arcsec) is centred on the light distribution and follows the semimajor axis. The other slits are 1 arcsec and 1.5 arcsec wide and are offset so as to be adjacent to the previous slit. The dotted red delineate the seven apertures with a width of 0.43 arcsec that were extracted from each longslit observation.

Figure 2. Extracted one-dimensional spectra for the central aperture of the 0.7-arcsec slit (left), 1-arcsec slit (centre) and 1.5-arcsec slit (right). The red line is the best-fitting model, the green line is the polynomial continuum model, and the lower panel shows the residuals. Greyed-out regions indicate parts of the spectra that were not included in the fit (two strong night-sky features, the Mg*b* line of SDSS J0728 and the O II features from the background source).
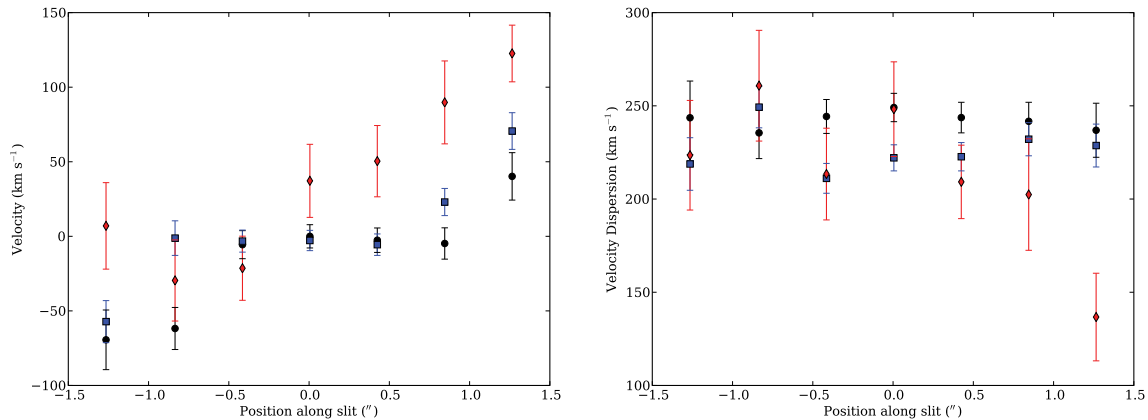
Figure 3. Line-of-sight velocity (left) and velocity dispersion (right) profiles for the lens SDSS J0728. The circles are for the central slit, the squares are for the slit offset 0.85 arcsec from the centre and the diamonds are for the widest slit offset 2.1 arcsec from the galaxy centre.
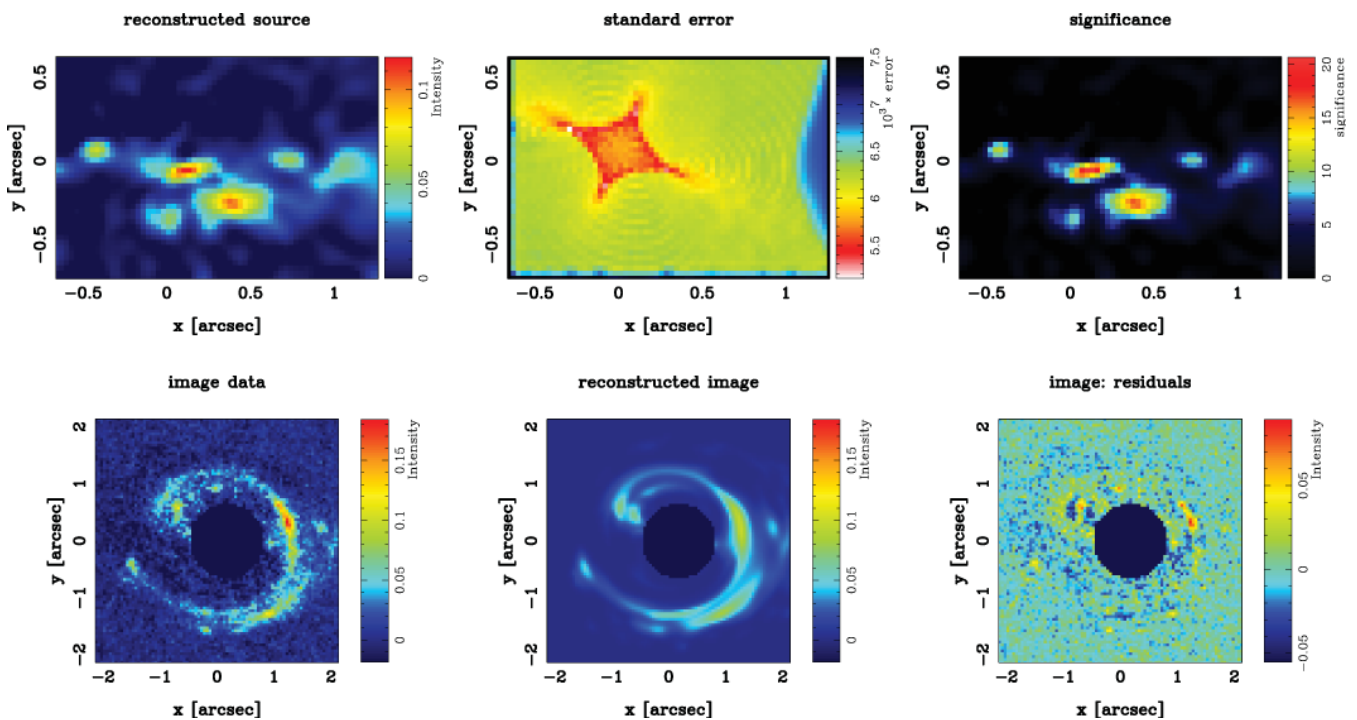

Figure 4. Best model lens image reconstruction for the system SDSS J0728. Top row: reconstructed source model; 1σ uncertainty on the source pixels; significance of the reconstructed source. Bottom row: *HST*/ACS data showing the lens image after subtraction of the lens galaxy; lens image reconstruction; residuals. In the panels, north is up and east is to the left.

3 ANALYSIS AND RESULTS

3.1 Joint gravitational lensing and stellar dynamics analysis

Here we briefly recall the general features of the CAULDRON code, the tool employed to carry out the combined self-consistent gravitational lensing and stellar dynamics analysis for the galaxy in question, SDSS J0728. The reader is referred to BK07 for a detailed description of the algorithm.

We characterize the lens galaxy by means of its total density distribution $\rho(\boldsymbol{\eta})$, where $\boldsymbol{\eta}$ is a set of parameters describing the density profile. Via the Poisson equation, we calculate the total gravitational potential Φ and use it simultaneously for both the gravitational lensing and the stellar dynamics modelling of the data set, which typically includes the surface brightness and velocity

moment maps of the lens galaxy and the surface brightness map of the lensed image. Both these modelling problems can be formalized as a set of regularized linear equations, for which standard solving techniques are readily available. Thus – given a combined data set – for each choice of the parameters $\boldsymbol{\eta}$ we can calculate the surface brightness distribution of the unlensed source and the weights of the elementary stellar dynamics building blocks. In order to determine the 'best' (in Occam's razor sense) density model given the data, this linear optimization scheme has been embedded within the framework of Bayesian statistics. This allows us to objectively quantify (and therefore rank) the plausibility of each model by means of the evidence merit function (see e.g. MacKay 1999, 2003). In this way, by maximizing the evidence, one recovers the set of non-linear parameters $\boldsymbol{\eta}$ corresponding to the best density model, i.e. the model which maximizes the joint posterior
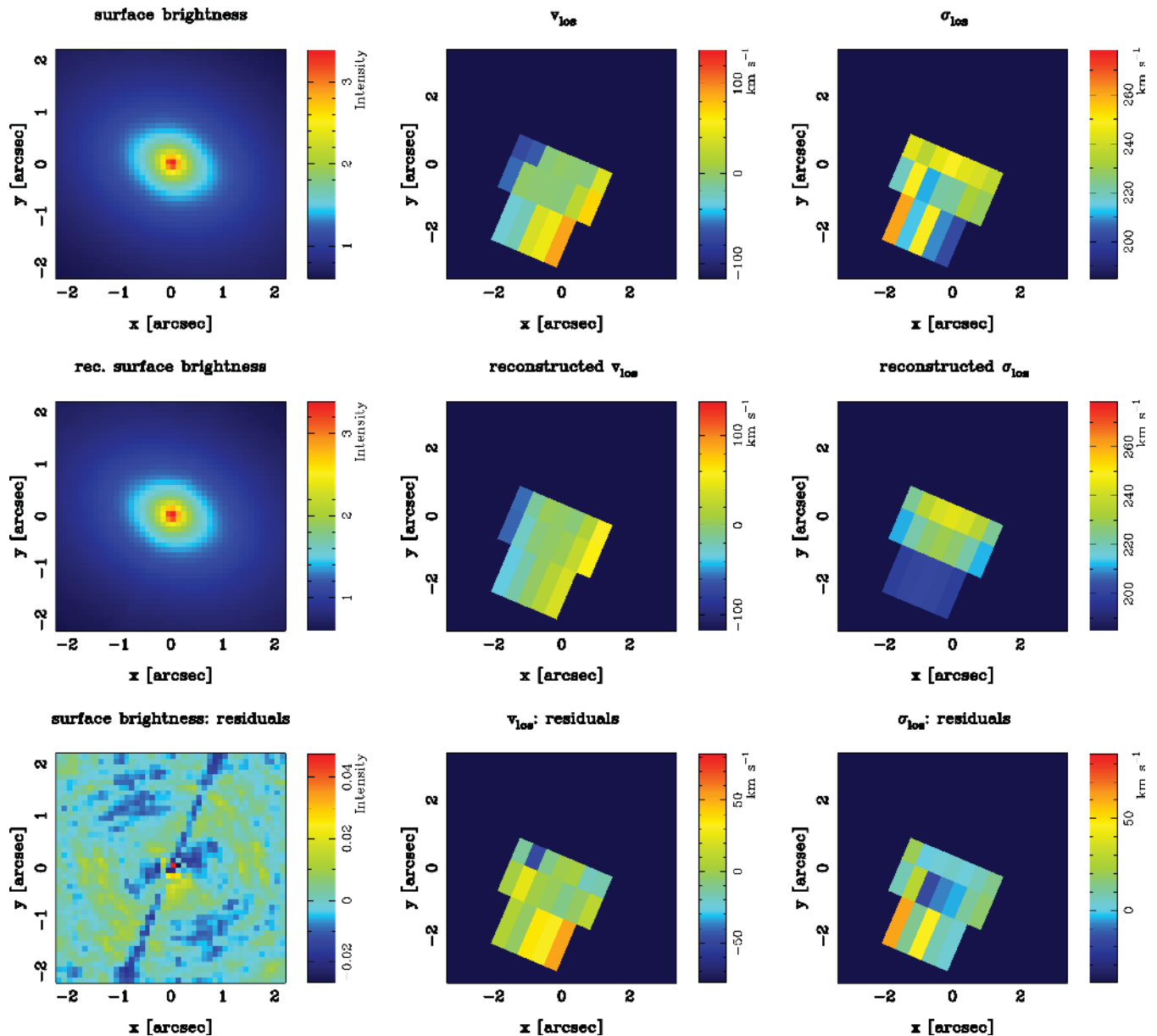
Figure 5. Best dynamical model for the galaxy SDSS J0728. Top row: observed surface brightness distribution, projected line-of-sight velocity and line-of-sight velocity dispersion. Middle row: corresponding reconstructed quantities for the best model. Bottom row: residuals. In the panels, north is up and east is to the left.

probability density function, hence called maximum *a posteriori* (MAP) model.

The method as described is extremely flexible and can in principle support any density profile, by adopting for example a completely general pixelized density distribution. However, its current practical implementation, the CAULDRON algorithm, is more restricted in order to make it computationally efficient and assumes axial symmetry [i.e. a density distribution of the form $\rho(R, z)$] and a two-integral stellar DF $f = f(E, L_z)$, where E and L_z denote the two classical integrals of motion, i.e. energy and angular momentum, respectively, along the rotation axis. As shown in BK07, under these assumptions it is possible to take advantage of a fast Monte Carlo numerical implementation of the two-integral Schwarzschild method described by Cretton et al. (1999) and Verolme & de Zeeuw (2002), which allows a dynamical model to be built in a matter of seconds and therefore makes it possible to explore large regions of the parameter space.

The distinguishing feature of this method is that the building blocks employed for the construction of the dynamical model are constituted by two-integral components (TICs) rather than stellar orbits as in the classical Schwarzschild method (Schwarzschild 1979; see e.g. Thomas et al. 2007b; van den Bosch et al. 2008 for modern implementations). A TIC can be visualized as an elementary toroidal system, completely specified by a particular choice of E and L_z. TICs have simple $1/R$ radial density distributions and analytic unprojected velocity moments, and by superposing them one can build $f(E, L_z)$ models for arbitrary spheroidal potentials (cf. Cretton et al. 1999): all these characteristics contribute to make TICs particularly valuable and inexpensive building blocks when compared to orbits.

Notwithstanding these restrictions, Barnabè et al. (2009a) have shown that CAULDRON works robustly even when applied to simulated systems which depart significantly from the method's assumptions (including the assumption of axial symmetry), reliably recovering

several important global properties of such systems, in particular the slope of the total mass density profile, which is determined within less than 10 per cent of the correct value. When the system displays rotation in the kinematical maps, as is the case for SDSS J0728, the main dynamical quantities (such as the global anisotropy parameter δ, the angular momentum and the ordered-to-random motions ratio; see Section 3.5) are recovered with an accuracy of 10–25 per cent.

3.2 The galaxy model

Stellar dynamics (e.g. Gerhard et al. 2001), strong and weak gravitational lensing (e.g. Gavazzi et al. 2007; Koopmans et al. 2009) and X-ray studies (see e.g. Humphrey & Buote 2010, and references therein) all concur in indicating that the total mass profile of elliptical galaxies is remarkably well described by a single power-law model over a large radial range.

As our model for the total mass density profile of the analysed lens galaxy, we adopt therefore an axially symmetric power-law distribution

$$\rho(m) = \frac{\rho_0}{m^{\gamma'}} \tag{1}$$

with ρ_0 being a density scale, $0 < \gamma' < 3$ the logarithmic slope of the density profile and m the elliptical radius, i.e.

$$m^2 = \frac{R^2}{a_0^2} + \frac{z^2}{c_0^2} = \frac{R^2}{a_0^2} + \frac{z^2}{a_0^2 q^2}, \tag{2}$$

where c_0 and a_0 are length-scales and the axial ratio $q \equiv c_0/a_0$. The corresponding (inner) gravitational potential $\Phi(R, z)$ associated with the distribution $\rho(m)$ can be obtained straightforwardly by means of the classical Chandrasekhar (1969) formula, which entails the computation of a single integral.

In case the assumption of a power-law density profile is an oversimplified description of the true mass distribution of the galaxy, this is expected to have visibly disrupting effects on the reconstructed observables, in particular for the lensing ones. As illustrated in the Barnabè et al. (2009a) tests, these can include a strongly irregular reconstructed source, with sharp transitions in intensity between close pixels (despite the usual adoption of a regularization term) and the presence of recognizable arc-like features in the lens image residuals. We emphasize, however, that such clear discrepancies have never surfaced in previous analyses of the SLACS systems (Czoske et al. 2008; B09), which support instead the effectiveness of the simple power-law model.

With this choice, the galaxy model is therefore characterized by three non-linear physical parameters, i.e. the slope γ', the axial ratio q and the dimensionless lens strength α_0, which is directly related to the normalization of the three-dimensional potential (see appendix B of BK07). To these, we must add the four 'geometrical' parameters defining the configuration of the system in the sky, i.e. the position angle ϑ_{PA}, the inclination i and the coordinates of the lens galaxy centre. The latter, as well as the angle ϑ_{PA}, are typically strongly constrained by the lens image brightness distribution and can be accurately determined by means of fast preliminary explorations and therefore kept fixed afterwards in order to decrease the number of free non-linear parameters during the more computationally expensive optimization and error analysis runs. If necessary, external shear can be also accounted for, by introducing shear strength and shear angle as additional parameters.

Finally, we have three so-called hyperparameters which control the level of the regularization in the reconstructed quantities: one for the surface brightness distribution of the unlensed source and two for the TIC weights map. Their values are set by optimizing the Bayesian posterior probability.

3.3 Uncertainties

In order to correctly assess the model uncertainties within the framework of Bayesian statistics, one needs to evaluate the posterior probability distribution of the parameters, i.e. by denoting the data set as d and the considered model or hypothesis as $\mathcal{H}$:

$$\mathcal{P}(\eta) \equiv \Pr(\eta|d, \mathcal{H}) \propto \mathcal{L}(\eta) \times p(\eta), \tag{3}$$

where $\mathcal{L}(\eta) \equiv \Pr(d|\eta, \mathcal{H})$ is the likelihood and $p(\eta) \equiv \Pr(\eta|\mathcal{H})$ is the prior. The individual parameter confidence intervals can be obtained by marginalizing the posterior over each of them.

Sampling a multidimensional distribution such as $\mathcal{P}$ is in general a challenging and computationally expensive task. An effective technique to tackle this problem is the nested sampling Monte Carlo method introduced by Skilling (2004) which, in calculating the evidence, produces posterior inferences as valuable by-products. For our error analysis, we make use of the MULTINEST algorithm developed by Feroz & Hobson (2008) and Feroz, Hobson & Bridges (2009), which provides an efficient and robust implementation of the nested sampling method and has been shown to yield reliable posterior inferences even in presence of multimodal and degenerate multivariate distributions.

The model parameters that we consider are the ones introduced in Section 3.2, i.e. the inclination i, the lens strength α_0, the slope γ' and the axial ratio q (the additional parameters which can be estimated by means of preliminary runs, such as the lens centre and the position angle, however, are kept fixed here in order to reduce the computational load) to which we must add the three hyperparameters. We formalize our ignorance by adopting flat priors (or flat in logarithm for the hyperparameters), constructed around the MAP value of each parameter and taken wide enough to include the bulk of posterior probability distribution. Finally, we conduct a thorough exploration of this seven-dimensional surface by launching MULTINEST with 400 live points,[1] from which the individual marginalized posterior probability distributions are obtained. In the following, we quote the 99 per cent confidence interval calculated from these distributions as our error.

3.4 Results for the best model reconstruction

The CAULDRON code has been applied to the combined data set described in Section 2. In order to avoid possible spurious effects in the lensing reconstruction, we have masked out the central regions of the lensed image map, where the residuals of the galaxy subtraction are still appreciable. We use the best-fitting B-spline model of the

---

[1] The live points (sometimes also called active points) are the initial samples drawn from the full prior distribution $p(\eta)$, from which the nested sampling exploration of the posterior is started. Our choice of 400 live points for the relatively well-behaved seven-dimensional distribution at hand is very conservative. In fact, as shown by the test problems examined in Feroz et al. (2009), 1000 or 2000 active points are sufficient for the application of MULTINEST even to, respectively, highly dimensional problems (with up to 30 parameters) or pathologically multimodal distributions (e.g. the egg-box likelihood presented in their section 6.1). Moreover, if one is more interested in determining the marginalized posterior distribution of the parameters rather than in accurately calculating the value of the total evidence, a much smaller number of live points (of the order of 50) is shown to be already enough to obtain a reliable estimate.

Table 1. Recovered model parameters for lens galaxy SDSS J0728.

Parameter	η_{MAP}	η_-	η_{max}	η_+
γ'	2.082	2.055	2.077	2.119
α_0	0.325	0.317	0.323	0.331
q	0.602	0.574	0.603	0.681
i	68.1	67.8	68.6	73.6

Note. The listed parameters are: the logarithmic slope γ', the dimensionless lens strength α_0, the axial ratio q and the inclination i (in degrees) with respect to the line of sight. The second column presents the MAP parameters, i.e. the parameters that maximize the joint posterior distribution. Columns 3–5 encapsulate a description of the one-dimensional marginalized posterior distributions, plotted in Fig. 6. The parameter η_{max} corresponding to the maximum of that distribution is listed in Column 4, while η_- and η_+ are, respectively, the lower and upper limits of the 99 per cent confidence interval.

lens galaxy as our data set for its surface brightness distribution, to avoid 'contamination' from the background galaxy lensed images, which is particularly bright and could bias the reconstructed model. A similar approach had been followed in the analysis of lens system SDSS J2321 (Czoske et al. 2008).

The recovered non-linear parameters for the best reconstructed model, i.e. the MAP model, are presented in Table 1. The uncertainties on the individual parameters are quantified by marginalizing, over each of them, the joint posterior distribution (see Fig. 6). The parameter values corresponding to the maximum of the one-dimensional marginalized posterior and the limits of the 99 per cent confidence interval are also listed in Table 1.

We find for SDSS J0728 a logarithmic slope $\gamma' = 2.077^{+0.042}_{-0.022}$ (errors indicate the 99 per cent confidence level), very close to the so-called isothermal (i.e. $\rho \sim 1/r^2$) profile which appears to be a characterizing feature of early-type galaxies, and in general agreement with previous combined lensing and dynamics studies of the SLACS sample (Koopmans et al. 2009; B09). For this specific system – by using the 3-arcsec aperture-averaged SDSS velocity

dispersion measure as the only kinematic constraint – Koopmans et al. (2009) determine a slightly different slope $\gamma' = 1.85 \pm 0.10$ (68 per cent CL), which, however, we find here to be too shallow to correctly reproduce the kinematic maps. One reason for this discrepancy is that the velocity dispersion derived from the SDSS is lower (typically of ~ 20 km s^{-1}) than the value obtained from Keck spectroscopy, as discussed in Section 2.2. Moreover, Koopmans et al. (2009) adopt a simpler dynamical model, based on solving spherical Jeans equations, which might have difficulties in describing a system characterized by a significant flattening like SDSS J0728.

The recovered lens strength is $\alpha_0 = 0.323^{+0.008}_{-0.006}$. The axial ratio of the total density distribution is found to be $q = 0.602^{+0.079}_{-0.028}$, slightly flatter than the intrinsic axial ratio $q_\star = 0.688$ of the luminous distribution, calculated by deprojecting the observed isophotal axial ratio $q_{\star,2D}$ by making use of the best model value $i = 68.6^{+5.0}_{-0.8}$ obtained for the inclination. Moreover, the position angle $\vartheta_{PA} = 67°.5$ is found to be extremely close to the value inferred from the light distribution, indicating alignment between the dark and luminous mass components in the inner regions of the galaxy.

The marginalized posterior probability distributions of these parameters (with the exception of the position angle, which, as previously described, is kept fixed after the preliminary run), as well as those of the regularization hyperparameters, obtained as described in Section 3.3, are shown in Fig. 6. We note that these represent the statistical errors on the considered power-law model and do not take into account the potential systematic uncertainties due to issues in the generation of the data sets (e.g. the procedure for galaxy subtraction, as pointed out by Marshall et al. 2007) or to incorrect model assumptions (as in the case of, e.g., non-axially symmetric density distribution or flattening that varies with radius). In the latter case, a quantitative estimate of the upper limits of the systematic errors can be obtained by looking at the findings of the Barnabè et al. (2009a) 'crash-test' where the CAULDRON code is applied to a
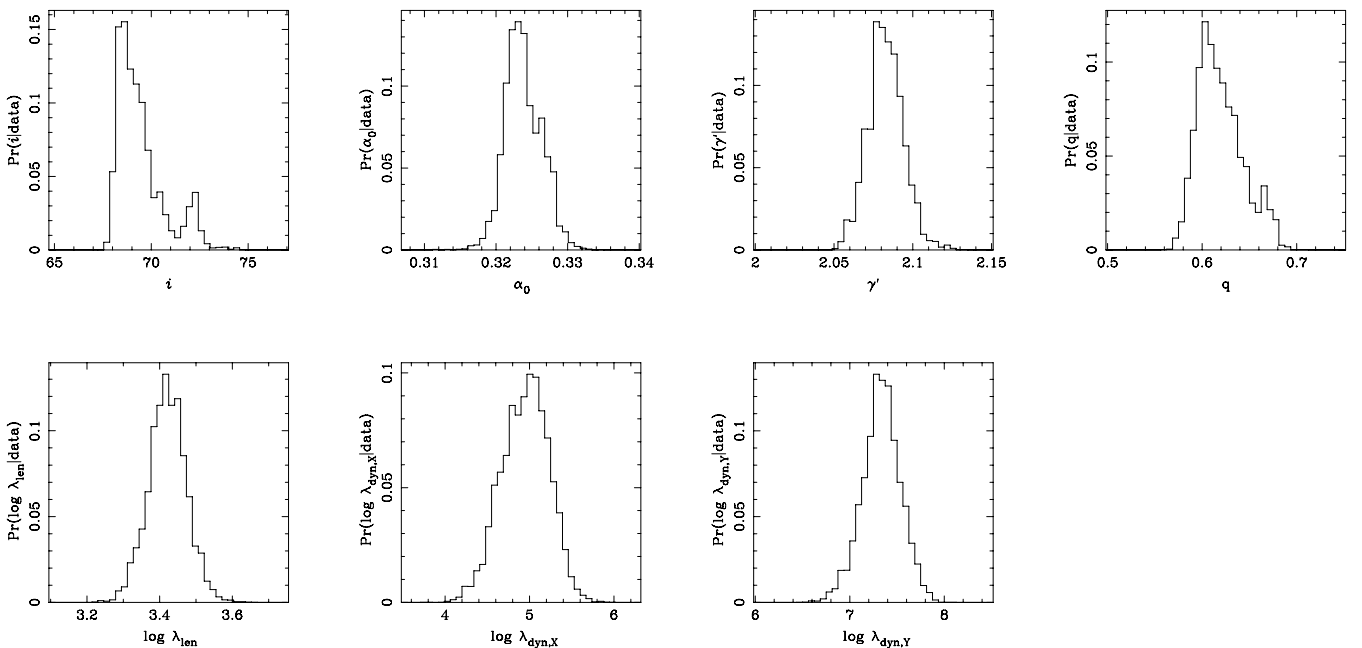

Figure 6. Marginalized posterior probability distributions of the power-law model parameters (inclination, lens strength, logarithmic slope and axial ratio) and hyperparameters, obtained from the nested sampling exploration of the posterior. The uncertainties on the parameters quoted in the text are calculated by considering the interval around the peak which contains 99 per cent of the probability.

non-symmetric simulated galaxy. As mentioned in Section 3.1, the error on the logarithmic slope γ' is less than 10 per cent even in this quite extreme case. Since real early-type galaxies are unlikely to depart from axisymmetry as drastically as this simulated system, we expect systematic uncertainties to remain within a few per cent level.

There is no evidence that any significant external shear effect needs to be included in order to model this system: when the external shear angle and strength are allowed to vary, the MAP model value of the latter is found to be negligibly small. This is consistent with the absence of massive structures near the lens galaxies found in Treu et al. (2009). We also explored the possibility of introducing a core radius in the density profile, without finding any improvement to justify the inclusion of this additional parameter.

In Figs 4 and 5 we present – respectively for lensing and dynamics – the SDSS J0728 data set, the reconstructed observables obtained for the MAP model and the corresponding residuals. This system displays an unusually structured lensed image, which we find to be produced by the presence of multiple components in the source plane. The reconstructed background source is shown in the top-left panel of Fig. 4; the top-middle and top-right panels show, respectively, the standard errors and the significance of the reconstructed source.

The surface brightness map is reconstructed very accurately. Since the adopted data set is a B-spline model and therefore noiseless, the small residuals (at the 1 per cent level) are dominated by the discreteness effects of the TIC superposition, which determines the concentric ripples, while the structure aligned with the galaxy minor axis is caused by the toroidal shape of the building blocks. These undesired effects have been kept under control by increasing both the number of TICs employed in the dynamical model (of almost a factor of 4, from $N_E = 10 \times N_{L_z} = 10$ elements adopted in the previous studies conducted with CAULDRON to 20×9 elements) and the number of particles populating each TIC. An additional and more compelling motivation for this improvement of the TIC library, which further justifies the increased computational burden, is that it proves to be important for the reconstruction of the kinematic observables (particularly the velocity dispersion map) at larger distances from the galaxy major axis, i.e. that part of our data set which best allows us to probe the system under study beyond the effective radius.

3.5 Global dynamical quantities

The recovered weighted stellar DF for the best combined model is presented in Fig. 7 as a map of the relative TIC weights over the integral space (E, L_z) (the grid in the radial coordinate R_c is related to a grid in energy as explained in BK07). This representation encodes, in a very compact way, much of the information on the dynamical structure of the galaxy that can be obtained under the assumptions of the adopted two-integral model. However, it is often useful to distil such information into quantities that allow for a more straightforward physical interpretation.

The global properties of the stellar velocity dispersion tensor are customarily encapsulated in the three anisotropy parameters

$$\beta \equiv 1 - \frac{\Pi_{zz}}{\Pi_{RR}}, \quad \gamma \equiv 1 - \frac{\Pi_{\varphi\varphi}}{\Pi_{RR}} \quad \text{and} \quad \delta \equiv 1 - \frac{2\Pi_{zz}}{\Pi_{RR} + \Pi_{\varphi\varphi}},$$

$$(4)$$

where we indicate with

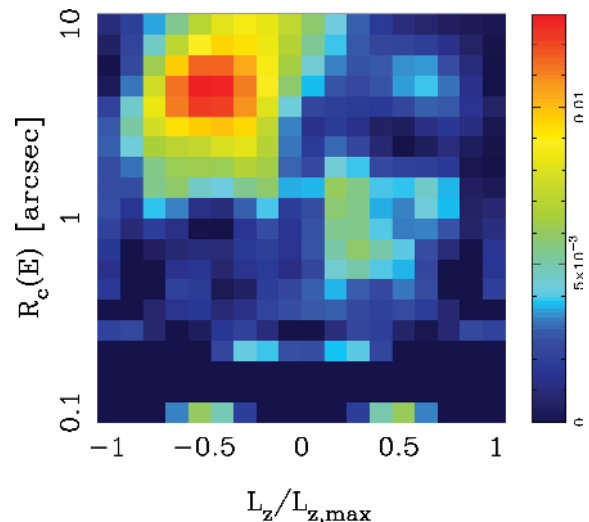$$\Pi_{kk} = \int \rho \sigma_k^2 \, \mathrm{d}^3\boldsymbol{x} \quad (5)$$

Figure 7. Reconstruction of the weighted two-integral DF of the system SDSS J0728 obtained from the MAP model. The value of each pixel in the two-integral space represents the relative contribution of the corresponding TIC to the stellar component of the modelled system.

the total unordered kinetic energy in the coordinate direction k and $\sigma_k(\boldsymbol{x})$ is the velocity dispersion along the direction k (see Cappellari et al. 2007; Binney & Tremaine 2008).

For SDSS J0728, we compute the integral of equation (5) within a cylinder of radius and height equal to R_e, i.e. inside a region which is very well constrained by the data, finding a mild anisotropy $\delta = 0.08 \pm 0.02$, which falls within the typical range of values for early-type galaxies both in the local Universe (Cappellari et al. 2007; Thomas et al. 2009) and up to redshift $z \sim 0.35$ (see B09). Since we make use of a two-integral DF dynamical model, the velocity dispersion tensor is isotropic in the meridional plane [i.e. $\sigma_R^2(\boldsymbol{x}) = \sigma_z^2(\boldsymbol{x})$ for each $\boldsymbol{x}$] and therefore $\beta \equiv 0$ by construction, and γ is univocally linked to δ by the relation $\gamma = 2\delta/(\delta - 1)$. For the analysed system, we have $\gamma = -0.18 \pm 0.04$.

The importance of rotation with respect to random motions is among the most defining aspects of the dynamical structure of a stellar system. In order to explore how this property varies with the position in the meridional plane, we calculate the local ratio $\langle v_\varphi \rangle / \bar{\sigma}$ of the mean rotation velocity around the z-axis to the mean velocity dispersion $\bar{\sigma}^2 \equiv (\sigma_R^2 + \sigma_\varphi^2 + \sigma_z^2)/3$ and we plot it in Fig. 8 up to 1 effective radius. The inner regions – within approximately 1 arcsec – are dominated by random motions, while rotation becomes more important at large radii, a trend somewhat reminiscent of what is found, in B09, for the fast rotator SDSS J0959 (although it should be remembered that the $\langle v_\varphi \rangle / \bar{\sigma}$ map of the latter only extends up to $R_e/2$). Not surprisingly, therefore, the presence of large-scale ordered motions is reflected also in the quite high value $j_z = 0.28^{+0.05}_{-0.01}$ obtained for the intrinsic rotation parameter, which is a dimensionless proxy for the galaxy angular momentum (refer to B09 for the definition).

3.6 Dark and luminous mass distribution

The spherically averaged profile of the galaxy total mass corresponding to the best reconstructed model (solid black curve in Fig. 9) can be calculated straightforwardly from equation (1), while the radial profile of the luminous component is obtained from the recovered stellar DF. However, since within our method stars are treated as tracers of the total potential, the normalization of the
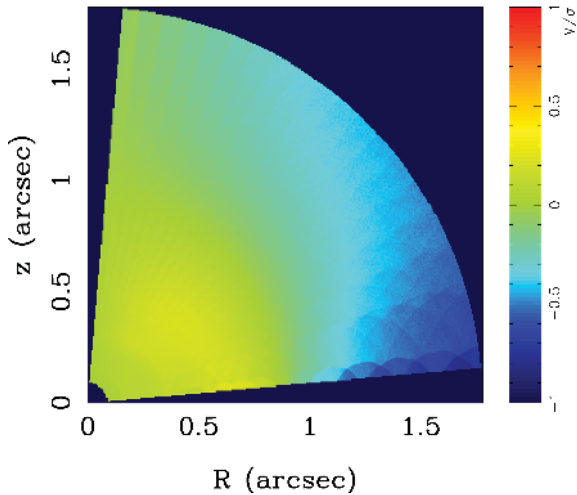
Figure 8. Map of the local $\langle v_\varphi \rangle / \bar{\sigma}$ ratio of the mean rotation velocity around the z-axis to the mean velocity dispersion, plotted up to R_e in the positive quadrant of the meridional plane.

luminous profile is not fixed and must be constrained by means of an independent determination of the stellar mass-to-light ratio or by introducing additional assumptions.

One particularly informative assumption, known as the 'maximum bulge' approach, consists in maximally rescaling the luminous mass distribution without exceeding the total mass profile at any radius. This provides a consistent and robust way to assess a lower limit for the dark matter fraction in the analysed system (under the hypothesis that the stellar mass-to-light ratio does not change too drastically with the position in the galaxy). By applying this procedure to SDSS J0728, we determine a value $\log(M_\star/M_\odot) = 11.50$ for the total stellar mass. With this normalization of the luminous mass profile, one finds a dark matter fraction of

16 per cent of the total mass within the (three-dimensional) spherical radius $r = R_e/2$, which rises to 28 per cent at $r = R_e$ – corresponding to about 6 kpc – and up to almost 40 per cent at $r \sim 10$ kpc, which is approximately the outer limit of the region over which we have direct information from the stellar kinematic maps. This result is consistent with the findings of purely dynamical studies of the inner regions of early-type galaxies in the local Universe (e.g. Gerhard et al. 2001; Cappellari et al. 2006; Thomas et al. 2007b). It is also in good agreement with the conclusions of our previous analysis of six SLACS lens systems (where the same maximum bulge prescription was adopted), for which, however, the kinematic data set does not extend beyond R_e, with the exception of galaxy SDSS J0959 (see B09). The corresponding upper limit for the stellar mass-to-light ratio in the B band of SDSS J0728 is $M_\star/L_B = 3.14$, which is in the lower end of the typical values reported for slow-rotating elliptical galaxies in the local Universe (Kronawitter et al. 2000; Gerhard et al. 2001; Trujillo, Burkert & Bell 2004). This is not too surprising, since the $M_\star/L_B$ is expected to increase by a significant amount (a factor of 1.4 according to Treu et al. 2002) between $z = 0.2$ and $z = 0$, simply due to passive evolution of stellar populations. More-over, the evidence of rotation at large radii (cf. Section 3.5) might indicate the presence of a disc component, typically characterized by a lower mass-to-light ratio.

It is interesting to compare this maximum bulge upper limit with the stellar masses determined from stellar population analysis. By applying a novel Bayesian stellar population analysis code to multiband imaging data, Auger et al. (2009) determine for galaxy SDSS J0728 – without including any priors from lensing – a value $\log(M_\star/M_\odot) = 11.44 \pm 0.12$ for a Chabrier (2003) IMF and a value $\log(M_\star/M_\odot) = 11.69 \pm 0.12$ for a Salpeter (1955) IMF (quoted errors are 1σ). We note that, since the thermally pulsing asymptotic giant branch stars do not dominate the luminosity of old stellar populations, the Bruzual & Charlot (2003) models used by Auger et al. (2009) should not be biased by ignoring them. In fact, the stellar masses for SLACS galaxies are found to be consistent with the
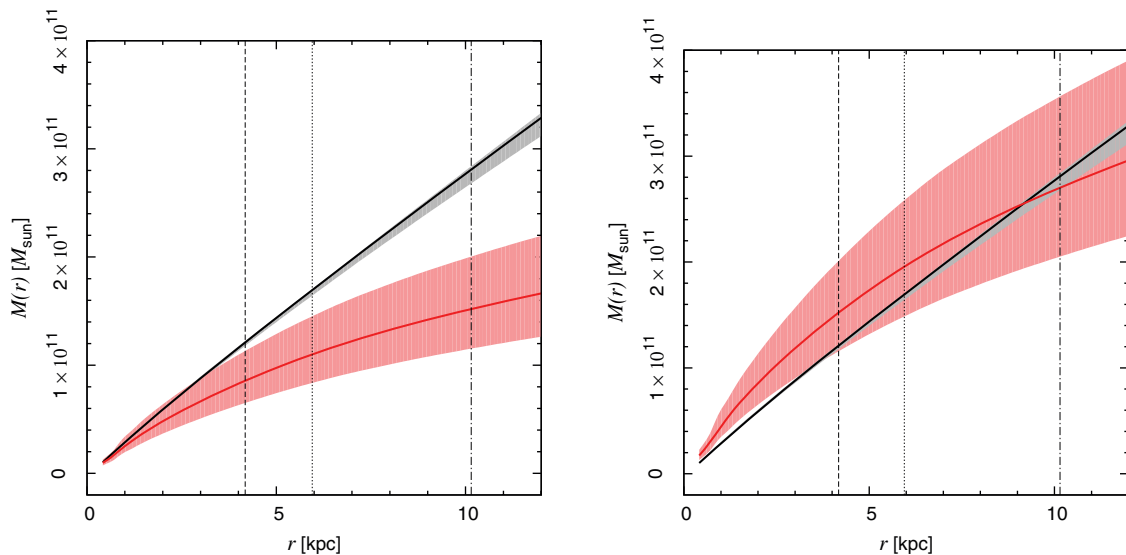

Figure 9. Spherically averaged mass distribution for lens galaxy SDSS J0728. The solid black line shows the total mass profile obtained from the best reconstructed model, with the statistical uncertainty represented as a grey band. The solid red line shows the luminous mass profile obtained from the recovered stellar DF and rescaled using the stellar masses obtained from the Auger et al. (2009) stellar population analysis with Chabrier and Salpeter IMFs (left-hand and right-hand panels, respectively); the upper and lower error bars quoted in that paper set the limits for the red-shaded regions. The vertical lines provide an indication of the region probed by the data set, showing the three-dimensional radius r which equals the Einstein radius (dashed line), the effective radius (dotted line) and the outermost boundary of the kinematic maps (dash–dotted line). See the online version of this article for a colour version of the figure.

masses determined from Maraston (2005) models (see Treu et al. 2010).

By using these stellar mass values to rescale the (spherically averaged) luminous profile, one obtains the red curves shown in Fig. 9. It can be clearly seen that the Salpeter IMF produces a stellar mass distribution which (unphysically) overshoots the total mass profile up to and beyond the effective radius. The Chabrier IMF, on the other hand, yields a physically acceptable luminous profile, which, interestingly, is also very close to the one determined through the maximum bulge assumption.

Treu et al. (2010) argue – based on the mass determinations from lensing, dynamics and stellar populations synthesis models for 56 SLACS systems – that early-type galaxies cannot have both universal IMF and dark matter profiles. In fact, if a universal Navarro, Frenk & White (NFW; Navarro, Frenk & White 1996, 1997) halo is assumed, the IMF shows a trend with velocity dispersion: a Chabrier-like normalization is more appropriate for less massive systems with σ of the order of 200 km s^{-1}, while more massive galaxies are better described with a Salpeter-like IMF. The results of our detailed analysis of SDSS J0728 are consistent with this general picture. With an SDSS velocity dispersion $\sigma = 214 \pm 11$ km s^{-1}, this system definitely belongs to the lower mass end of the SLACS sample, and its halo profile is consistent with NFW (as discussed in Section 3.7). Clearly, since this conclusion is based on only one system, a full analysis of the sample still needs to be done to further strengthen this tentative trend.

3.7 Is the isothermal profile consistent with an NFW halo?

The combined analysis of SDSS J0728 has provided us with the total mass density profile of this galaxy within its inner regions. As discussed in the previous section, and visualized in Fig. 9, the luminous component alone cannot account for this mass profile over the entire radial range, even if its contribution is maximized (unless the stellar mass-to-light ratio changes with radius in a very fine-tuned manner). One therefore needs to invoke an additional mass component characterized by the specific profile that complements the luminous distribution. Interestingly, we find that the mass distribution of this dark component can be consistent with an NFW halo profile.

To show this, we attempt to describe the (spherically averaged) total mass distribution of the galaxy as the sum of the luminous component, calculated as before from the recovered stellar DF, and a dark component modelled as a standard NFW halo, i.e.

$$\rho_{\mathrm{NFW}}(r) = \frac{\rho_{\mathrm{crit}}\delta_c}{(r/r_{\mathrm{b}})\,(1 + r/r_{\mathrm{b}})^2}\,, \qquad (6)$$

where ρ_{crit} is the critical density, the characteristic overdensity of the halo δ_c is a dimensionless parameter connected to the halo concentration c by the relation

$$\delta_c = \frac{200}{3}\,\frac{c^3}{[\ln(1+c) - c/(1+c)]} \qquad (7)$$

and r_{b} denotes the break radius. We adopt $r_{\mathrm{b}} = 25$ kpc, based on the Gavazzi et al. (2007) weak lensing analysis of the SLACS sample and the consideration that SDSS J0728 is slightly less massive than the average SLACS system (for which $\langle\sigma_{\mathrm{SDSS}}\rangle \simeq 250$ km s^{-1}).

We then determine the (non-negative) normalization coefficients for the dark and luminous distribution which allow us to best reproduce (in a least-squares sense) the total mass profile of the galaxy. Remarkably – despite the fact that the only two free parameters here are the rescaling factors – the superposition of these two simple components proves to be enough to reproduce the total profile
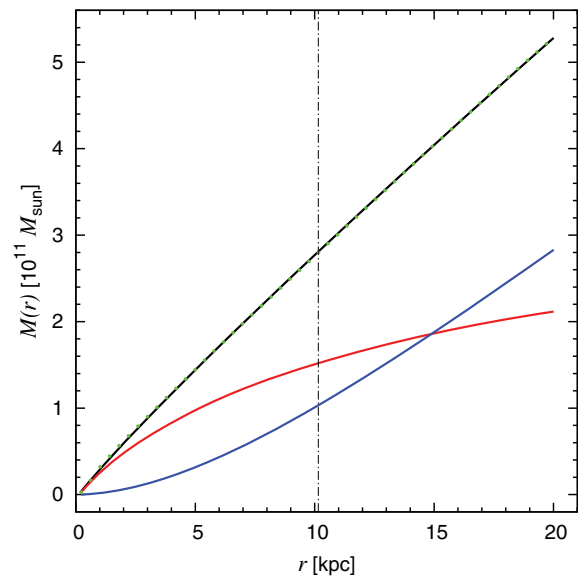

Figure 10. Best-fitting decomposition of the total mass profile of SDSS J0728 (black curve) in the sum of an NFW dark matter halo with break radius $r_{\mathrm{b}} = 25$ kpc (blue curve) and the luminous profile obtained from the recovered stellar DF (red curve). The dotted green line which very closely matches the black curve over the whole radial interval is the profile obtained by adding up the luminous and dark components. The vertical dash–dotted line indicates the outermost boundary of the kinematic maps. See the online version of this article for a colour version of the figure.

with great accuracy over the whole radial range covered by the observations, as shown in Fig. 10. Moreover, the combined profile remains consistent with the one predicted by a nearly isothermal density distribution even beyond 10 kpc and up to the break radius.

The luminous profile obtained in this way almost coincides with the one determined by means of the maximum bulge approach, with $\log(M_\star/M_\odot) = 11.50$, while the normalization for the dark halo profile translates into a concentration parameter $c \simeq 11$, from which one infers a virial radius $r_{200} = cr_{\mathrm{b}} \simeq 280$ kpc and a halo mass $M_{200} \simeq 3.1 \times 10^{12}\,M_\odot$. This is a mildly high value for the concentration when compared with the range $c \sim 3$–10 obtained from numerical simulations of relaxed dark matter haloes of corresponding mass (see in particular Macciò, Dutton & van den Bosch 2008). However, concentrations higher than the theoretical predictions are found in dynamical studies of slow-rotating early-type galaxies (see e.g. Romanowsky 2010, and references therein). We note that, in our case, lower concentrations are obtained by setting a larger value for the break radius, e.g. $c \sim 10$ for $r_{\mathrm{b}} = 30$ kpc, while the fit to the total mass profile becomes only slightly worse, with discrepancy of a few per cent.

4 CONCLUSIONS

We have carried out a detailed study of the mass profile and dynamical structure of the inner regions of the early-type lens galaxy SDSS J0728, located at a redshift $z = 0.21$, using a composite data set consisting of *HST*/Advanced Camera for Surveys (ACS) high-resolution imaging and two-dimensional kinematic maps constructed from long-slit spectroscopic observations obtained with the Keck instrument LRIS (the slit – aligned with the galaxy major axis – has been positioned at three different heights along the minor axis, allowing us to mimic integral-field spectroscopy). We have modelled the system by making use of the CAULDRON code for combined

gravitational lensing and stellar dynamics analysis, which operates under the assumptions of axial symmetry and two-integral stellar DF. With respect to sample studies of the SLACS lens galaxies such as Koopmans et al. (2009), the approach used here presents a number of improvements: it employs a self-consistent framework where the same total potential is used for both lensing and dynamics, it allows one to construct genuine axisymmetric dynamical models (albeit restricted to two integrals of motions) and it extracts much more information from the data set, making use – in addition to the lensed image – of the lens galaxy surface brightness and velocity moment maps rather than being limited to a single measure of the SDSS velocity dispersion. This permits a much greater level of detail to be recovered when modelling the system.

SDSS J0728 is the first galaxy for which it has been possible to conduct this kind of in-depth combined analysis by taking advantage of a kinematic data set that extends well past the effective radius: the outermost pixels of the velocity moment maps probe a region up to a distance of about 3 arcsec from the centre, corresponding to $\sim 1.7 R_e$. For comparison, in the sample of six SLACS lens galaxies examined in B09, the outermost boundary R_{kin} of the kinematic maps (obtained with VLT VIMOS integral-field spectroscopy) is in the range of 0.30–0.85R_e, with the single exception of system SDSS J0959 for which R_{kin} exceeds the effective radius of about 15 per cent.

The main results of the analysis are summarized and discussed below.

(i) The total mass density profile of the galaxy inner regions, up to a radius of $\sim 1.7 R_e$, is found to be satisfactorily described by a simple axisymmetric distribution $\rho \propto 1/m^{\gamma'}$, with a logarithmic slope $\gamma' = 2.08^{+0.04}_{-0.02}$ (99 per cent CL). This is very close to the isothermal profile (i.e. $\rho \propto 1/m^2$), which seems to be a ubiquitous characteristic of early-type galaxies at least up to redshift $z \sim 1$, as revealed by a number of dynamics, X-ray and combined lensing and dynamics studies (see e.g. Kronawitter et al. 2000; Gerhard et al. 2001; Humphrey & Buote 2010; Koopmans et al. 2009 and references therein). Moreover, weak lensing studies show that the total density profile remains consistent with being isothermal also well beyond the galaxy inner regions, up to radial distances of about 100 effective radii (Gavazzi et al. 2007).

The physical mechanisms which cause the total density distribution to be shaped into this particular structure, with little but non-negligible intrinsic scattering ($\lesssim 10$ per cent in γ'; see B09; Koopmans et al. 2009), are not well understood. The apparent 'conspiracy' between the luminous and dark components to generate a nearly isothermal combined profile appears even more surprising when considering that numerical simulations including gas dynamics find dark matter density profiles which depend both on the number of baryons and on the details of the assembly processes (see e.g. Abadi et al. 2009; Tissera et al. 2010).

Interestingly, despite the predicted complications, for SDSS J0728 we find that it is possible to reproduce very accurately the (spherically averaged) total mass distribution by combining two very intuitive and simple building blocks: (1) the luminous mass profile obtained from the stellar DF, almost maximally rescaled, and (2) an NFW dark matter halo (with a break radius $r_b = 20$ kpc and a concentration parameter $c \sim 14$).

(ii) We find the total density distribution to be quite flattened within the probed region, with an axial ratio $q = 0.60^{+0.08}_{-0.03}$, which is flatter than the axial ratio $q_\star$ of the luminous distribution (obtained by using the best model recovered inclination to deproject the two-dimensional isophotal axial ratio). This characteristic differentiates

SDSS J0728 from the six lens galaxies studied in B09, for which $q/q_\star \gtrsim 1$.

(iii) The system is characterized by a very mild anisotropy $\delta = 0.08 \pm 0.02$. On examining the dynamical structure of the galaxy by means of the $\langle v_\varphi \rangle / \bar{\sigma}$ map, one notes that the contribution of ordered motions becomes more important outside the inner regions, which determines the moderately high value $j_z = 0.28$ for the dimensionless angular momentum parameter. This result is obtained by integrating within a cylindrical region of radius and height equal to R_e. If the integration is limited to $R_e/2$, in order to allow a direct comparison with results of B09, one finds a lower $j_z = 0.18$, fully consistent with the typical values obtained for the galaxies in that sample (with the exception of the clearly fast-rotating SDSS J0959).

(iv) Under the assumptions of maximum bulge and position-independent stellar mass-to-light ratio, we determine for the dark matter fraction a lower limit of 28 per cent within the spherical radius $r = R_e$. Within $r \sim 10$ kpc, i.e. the approximate extension of the area directly probed by the kinematic data, the contribution of the dark matter to the total cumulative mass is about 40 per cent, almost matching the luminous component. This is in agreement with the findings of dynamical studies of nearby ellipticals (Gerhard et al. 2001; Cappellari et al. 2006; Thomas et al. 2007a) as well as with the combined lensing and dynamics analysis of six SLACS galaxies at $z = 0.08$–0.33 (Czoske et al. 2008; B09). Interestingly, numerical simulations of early-type galaxy formation from cosmological initial conditions also predict a dark matter fraction of about 20–40 per cent within this radius (Naab et al. 2007).

In alternative to the previous approach, we have also rescaled the luminous profile by using the stellar masses calculated from the Auger et al. (2009) stellar population analysis. The obtained luminous mass distribution is too high in the case of a Salpeter IMF, exceeding the total mass in places, while for a Chabrier IMF it remains lower than $M_{tot}(r)$ and, moreover, close to the profile predicted under the maximum bulge hypothesis. This suggests, in agreement with the conclusions of Treu et al. (2010), that a Chabrier functional form might be more suited to describe the IMF for less massive early-type galaxies such as SDSS J0728.

In order to further test if this description is correct, we plan to extend this study to a wider sample of SLACS lens galaxies, covering a broad range of velocity dispersions $\sigma \approx 200$–350 km s^{-1}, for which two-dimensional kinematic data sets are available.

In conclusion, despite being located at a redshift greater than 0.2, the system SDSS J0728 shows structural characteristics – namely nearly isothermal total density profile, dark matter fraction, anisotropy parameter δ, local ratio of ordered to random motions – broadly consistent with what is observed in the nearby Universe for early-type galaxies of comparable luminosity and velocity dispersion (e.g. Gerhard et al. 2001; Cappellari et al. 2007; Thomas et al. 2007a). The upper limit for the B-band stellar mass-to-light ratio, obtained from the maximum bulge assumption, is also in line with the values determined for local ellipticals (e.g. Kronawitter et al. 2000), once the ageing of the stellar populations is taken into account. This study therefore provides an indication that the density profile as well as the global dynamical structure of the inner regions of massive ellipticals did not undergo any dramatic change or significant evolution across the last two billion years.

REFERENCES

Abadi M. G., Navarro J. F., Fardal M., Babul A., Steinmetz M., 2009, preprint (arXiv:0902.2477)

Auger M. W., Treu T., Bolton A. S., Gavazzi R., Koopmans L. V. E., Marshall P. J., Bundy K., Moustakas L. A., 2009, ApJ, 705, 1099

Barnabè M., Koopmans L. V. E., 2007, ApJ, 666, 726 (BK07)

Barnabè M., Nipoti C., Koopmans L. V. E., Vegetti S., Ciotti L., 2009a, MNRAS, 393, 1114

Barnabè M., Czoske O., Koopmans L. V. E., Treu T., Bolton A. S., Gavazzi R., 2009b, MNRAS, 399, 21 (B09)

Binney J., Tremaine S., 2008, Galactic Dynamics. Princeton Univ. Press, Princeton, NJ

Bolton A. S., Burles S., Koopmans L. V. E., Treu T., Moustakas L. A., 2006, ApJ, 638, 703

Bolton A. S., Burles S., Koopmans L. V. E., Treu T., Gavazzi R., Moustakas L. A., Wayth R., Schlegel D. J., 2008a, ApJ, 682, 964

Bolton A. S., Treu T., Koopmans L. V. E., Gavazzi R., Moustakas L. A., Burles S., Schlegel D. J., Wayth R., 2008b, ApJ, 684, 248

Borriello A., Salucci P., Danese L., 2003, MNRAS, 341, 1109

Bruzual G., Charlot S., 2003, MNRAS, 344, 1000

Cappellari M. et al., 2006, MNRAS, 366, 1126

Cappellari M. et al., 2007, MNRAS, 379, 418

Chabrier G., 2003, PASP, 115, 763

Chandrasekhar S., 1969, Ellipsoidal Figures of Equilibrium. Yale Univ. Press, New Haven

Côté P., McLaughlin D. E., Cohen J. G., Blakeslee J. P., 2003, ApJ, 591, 850

Cretton N., de Zeeuw P. T., van der Marel R. P., Rix H.-W., 1999, ApJS, 124, 383

Czoske O., Barnabè M., Koopmans L. V. E., Treu T., Bolton A. S., 2008, MNRAS, 384, 987

de Lorenzi F., Gerhard O., Saglia R. P., Sambhus N., Debattista V. P., Pannella M., Méndez R. H., 2008, MNRAS, 385, 1729

Falco E. E., Gorenstein M. V., Shapiro I. I., 1985, ApJ, 289, L1

Feroz F., Hobson M. P., 2008, MNRAS, 384, 449

Feroz F., Hobson M. P., Bridges M., 2009, MNRAS, 398, 1601

Franx M., van Gorkom J. H., de Zeeuw T., 1994, ApJ, 436, 642

Fukazawa Y., Botoya-Nonesa J. G., Pu J., Ohto A., Kawano N., 2006, ApJ, 636, 698

Fukugita M., Hogan C. J., Peebles P. J. E., 1998, ApJ, 503, 518

Gavazzi R., Treu T., Rhodes J. D., Koopmans L. V. E., Bolton A. S., Burles S., Massey R. J., Moustakas L. A., 2007, ApJ, 667, 176

Gavazzi R., Treu T., Koopmans L. V. E., Bolton A. S., Moustakas L. A., Burles S., Marshall P. J., 2008, ApJ, 677, 1046

Gerhard O. E., 1993, MNRAS, 265, 213

Gerhard O., Kronawitter A., Saglia R. P., Bender R., 2001, AJ, 121, 1936

Grillo C., Eichner T., Seitz S., Bender R., Lombardi M., Gobat R., Bauer A., 2010, ApJ, 710, 372

Humphrey P. J., Buote D. A., 2010, MNRAS, 403, 2143

Humphrey P. J., Buote D. A., Gastaldello F., Zappacosta L., Bullock J. S., Brighenti F., Mathews W. G., 2006, ApJ, 646, 899

Jiang G., Kochanek C. S., 2007, ApJ, 671, 1568

Kochanek C. S., 1991, ApJ, 373, 354

Koopmans L. V. E., Treu T., 2002, ApJ, 568, L5

Koopmans L. V. E., Treu T., 2003, ApJ, 583, 606

Koopmans L. V. E., Treu T., Bolton A. S., Burles S., Moustakas L. A., 2006, ApJ, 649, 599

Koopmans L. V. E. et al., 2009, ApJ, 703, L51

Kronawitter A., Saglia R. P., Gerhard O., Bender R., 2000, A&AS, 144, 53

Loewenstein M., White R. E., 1999, ApJ, 518, 50

Łokas E. L., Mamon G. A., 2003, MNRAS, 343, 401

Macciò A. V., Dutton A. A., van den Bosch F. C., 2008, MNRAS, 391, 1940

MacKay D. J. C., 1999, Neural Comput., 11, 1035

MacKay D. J. C., 2003, Information Theory, Inference and Learning Algorithms. Cambridge Univ. Press, Cambridge

Maraston C., 2005, MNRAS, 362, 799

Marshall P. J. et al., 2007, ApJ, 671, 1196

Matsushita K., Makishima K., Ikebe Y., Rokutanda E., Yamasaki N., Ohashi T., 1998, ApJ, 499, L13

Naab T., Johansson P. H., Ostriker J. P., Efstathiou G., 2007, ApJ, 658, 710

Navarro J. F., Frenk C. S., White S. D. M., 1996, ApJ, 462, 563

Navarro J. F., Frenk C. S., White S. D. M., 1997, ApJ, 490, 493

Oke J. B. et al., 1995, PASP, 107, 375

Padmanabhan N. et al., 2004, New Astron., 9, 329

Rix H.-W., de Zeeuw P. T., Cretton N., van der Marel R. P., Carollo C. M., 1997, ApJ, 488, 702

Romanowsky A. J., 2010, in Debattista V. P., Popescu C. C., eds, AIP Conf. Proc. Vol. 1240, Hunting for the Dark: The Hidden Side of Galaxy Formation. Am. Inst. Phys., New York, in press

Romanowsky A. J., Douglas N. G., Arnaboldi M., Kuijken K., Merrifield M. R., Napolitano N. R., Capaccioli M., Freeman K. C., 2003, Sci, 301, 1696

Rusin D., Kochanek C. S., 2005, ApJ, 623, 666

Saglia R. P., Bertin G., Stiavelli M., 1992, ApJ, 384, 433

Salpeter E. E., 1955, ApJ, 121, 161

Schwarzschild M., 1979, ApJ, 232, 236

Skilling J., 2004, in Fischer R., Preuss R., Toussaint U. V., eds, AIP Conf. Proc. Vol. 735, 24th International Workshop on Bayesian Inference and Maximum Entropy Methods in Science and Engineering. Am. Inst. Phys., New York, p. 395

Suyu S. H., Marshall P. J., Auger M. W., Hilbert S., Blandford R. D., Koopmans L. V. E., Fassnacht C. D., Treu T., 2010, ApJ, 711, 201

Thomas J., Jesseit R., Naab T., Saglia R. P., Burkert A., Bender R., 2007a, MNRAS, 381, 1672

Thomas J., Saglia R. P., Bender R., Thomas D., Gebhardt K., Magorrian J., Corsini E. M., Wegner G., 2007b, MNRAS, 382, 657

Thomas J. et al., 2009, MNRAS, 393, 641

Tissera P. B., White S. D. M., Pedrosa S., Scannapieco C., 2010, MNRAS, in press (doi:10.1111/j.1365-2966.2010.16777.x)

Tortora C., Napolitano N. R., Romanowsky A. J., Capaccioli M., Covone G., 2009, MNRAS, 396, 1132

Treu T., Koopmans L. V. E., 2002a, MNRAS, 337, L6

Treu T., Koopmans L. V. E., 2002b, ApJ, 575, 87

Treu T., Koopmans L. V. E., 2004, ApJ, 611, 739

Treu T., Stiavelli M., Casertano S., Møller P., Bertin G., 2002, ApJ, 564, L13

Treu T., Koopmans L. V. E., Bolton A. S., Burles S., Moustakas L., 2006, ApJ, 640, 662

Treu T., Gavazzi R., Gorecki A., Marshall P. J., Koopmans L. V. E., Bolton A. S., Moustakas L. A., Burles S., 2009, ApJ, 690, 670

Treu T., Auger M. W., Koopmans L. V. E., Gavazzi R., Marshall P. J., Bolton A. S., 2010, ApJ, 709, 1195

Trott C. M., Treu T., Koopmans L. V. E., Webster R. L., 2010, MNRAS, 401, 1540

Trujillo I., Burkert A., Bell E. F., 2004, ApJ, 600, L39

Turner E. L., Ostriker J. P., Gott J. R., III, 1984, ApJ, 284, 1

van de Ven G., Falcon-Barroso J., McDermid R. M., Cappellari M., Miller B. W., de Zeeuw P. T., 2008, preprint (arXiv:0807.4175)

van den Bosch R. C. E., van de Ven G., Verolme E. K., Cappellari M., de Zeeuw P. T., 2008, MNRAS, 385, 647

van der Marel R. P., Franx M., 1993, ApJ, 407, 525

Verolme E. K., de Zeeuw P. T., 2002, MNRAS, 331, 959

Warren S. J., Dye S., 2003, ApJ, 590, 673

Weijmans A., Krajnović D., van de Ven G., Oosterloo T. A., Morganti R., de Zeeuw P. T., 2008, MNRAS, 383, 1343

Weijmans A. et al., 2009, MNRAS, 398, 561

Wucknitz O., 2002, MNRAS, 332, 951

This paper has been typeset from a TEX/LATEX file prepared by the author.